Research Square

Preprints are preliminary reports that have not undergone peer review.
They should not be considered conclusive, used to inform clinical practice,
or referenced by the media as validated information.

Biogenic Vanadium Pentoxide Nanoparticles from Parmentiera cereifera for Biological Activity and Green Metrics Evaluation

Naveen Pathivada[1]

naveen.sklm@gmail.com

Government Degree College (Autonomous)

Gopi Mamidi[2]

Dr. VSK Government Degree College

AmanCharla Indira Priyadarsini[3]

Government Degree College (Autonomous)

Gunduluru Swathi[4]

Government Degree College (Autonomous),

Research Article

Keywords:

Posted Date: May 13th, 2026

DOI: https://doi.org/10.21203/rs.3.rs-9468447/v1

License: This work is licensed under a Creative Commons Attribution 4.0 International License.
Read Full License

Additional Declarations: No competing interests reported.

Biogenic Vanadium Pentoxide Nanoparticles from Parmentiera cereifera for Biological Activity and Green Metrics Evaluation

Naveen Pathivada[1]*, Gopi Mamidi[2], AmanCharla Indira Priyadarsini[3], Gunduluru Swathi[4]

[1] Government Degree College (Autonomous), Nagari, Chittoor, Andhra Pradesh, India
[2] Dr. VSK Government Degree College, Visakhapatnam, Andhra Pradesh, India
[3] Government Degree College (Autonomous), Nagari, Chittoor, Andhra Pradesh, India
[4] Government Degree College (Autonomous), Nagari, Chittoor, Andhra Pradesh, India

***Corresponding author: naveen.sklm@gmail.com**

Naveen Pathivada[1]*, naveen.sklm@gmail.com, https://orcid.org/0009-0003-1664-1988

Dr. Gopi Mamidi[2], naveenpathivada@gmail.com , https://orcid.org/0009-0009-1248-7745

Dr. AmanCharla Indira Priyadarsini[3], pnani0856@gmail.com, https://orcid.org/0009-0005-3118-2024

Dr. Gunduluru Swathi[4], chemistrydept@gdcnagari.edu.in, https://orcid.org/0009-0005-9008-9532

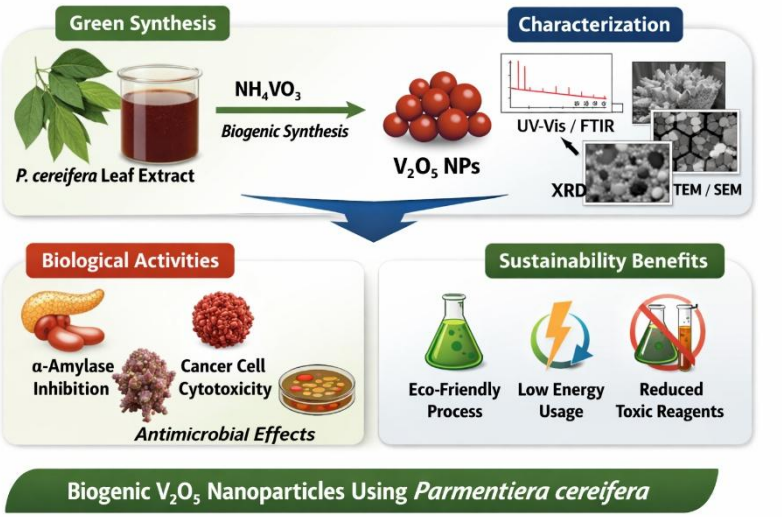

Abstract

Green nanotechnology offers a sustainable alternative to conventional synthesis of metal and metal-oxide nanomaterials by minimizing toxic reagents and energy consumption. Among these, vanadium pentoxide (V_2O_5) has attracted considerable interest due to its catalytic and biomedical properties; however, environmentally benign synthesis routes remain limited. In this study, V_2O_5 nanoparticles were synthesized for the first time using aqueous leaf extract of *Parmentiera cereifera*, establishing a previously unexplored plant–metal system. The plant extract served as both reducing and stabilizing agent for the conversion of ammonium metavanadate (NH_4VO_3) into V_2O_5 nanoparticles under mild conditions (70 °C, near-neutral pH). The resulting nanoparticles were characterized using UV–visible spectroscopy, FTIR, XRD, SEM, TEM, EDX, and zeta

potential analysis. Their biological activities, including α-amylase inhibition, cytotoxicity, and antimicrobial efficacy, were evaluated alongside sustainability metrics. The synthesized nanoparticles exhibited a characteristic absorption band at ~320 nm and distinct V–O/V=O vibrations, confirming V_2O_5 formation. XRD analysis revealed an orthorhombic crystalline phase with an average crystallite size of ~45 ± 5 nm, while microscopy showed quasi-spherical particles in the 20–60 nm range. A zeta potential of −28.4 mV indicated good colloidal stability. Functionally, the nanoparticles demonstrated concentration-dependent α-amylase inhibition (IC_{50} ≈ 38.4 µg mL^{-1}), selective cytotoxicity toward A549 cells, and broad-spectrum antimicrobial activity against *Staphylococcus aureus*, *Escherichia coli*, and *Candida albicans*. In addition, the process achieved a significant reduction in chemical usage and energy demand compared to conventional methods.Overall, this study introduces *Parmentiera cereifera* as a novel biogenic resource for V_2O_5 nanoparticle synthesis and presents a reproducible, environmentally compatible approach with potential biomedical relevance. Further studies focusing on mechanistic validation and in vivo evaluation are warranted.

1. Introduction

1. Introduction

Nanotechnology has significantly advanced materials science by enabling the design and control of materials at the nanoscale, leading to properties that differ from their bulk counterparts [1–3]. Metal and metal oxide nanoparticles, in particular, have attracted considerable attention due to their applications in catalysis, sensing, environmental remediation, and biomedical fields [4–6]. However, conventional synthesis methods such as sol–gel, hydrothermal, and chemical reduction techniques often rely on toxic reagents, organic solvents, and high energy input, which raise environmental and safety concerns [7–10]. To address these limitations, green nanotechnology has emerged as a sustainable alternative, emphasizing the use of non-toxic reagents, mild reaction conditions, and renewable biological resources [3,11–13]. Among these approaches, plant-mediated synthesis has gained prominence due to its simplicity, cost-effectiveness, and scalability [14–16]. Plant extracts are rich in phytochemicals such as polyphenols, flavonoids, terpenoids, and reducing sugars, which can act as both reducing and stabilizing agents during nanoparticle formation [17–19]. These biomolecules facilitate the reduction of metal ions and simultaneously prevent aggregation, resulting in stable and biocompatible nanostructures [20–22]. Among transition metal oxides, vanadium oxides (V_2O_5, VO_2, V_2O_3) are of particular interest due to their multiple oxidation states and redox flexibility [23–25]. Vanadium pentoxide (V_2O_5), in particular, exhibits a layered orthorhombic structure that supports applications in catalysis, energy storage, and sensing [26–28]. In addition to these physicochemical properties, vanadium-based nanomaterials have shown potential biological activity, including antidiabetic, anticancer, and antimicrobial effects [29–31]. These effects are generally associated with redox activity and the ability to influence cellular processes such as oxidative stress and metabolic pathways [32–34]. However, conventional synthesis routes for V_2O_5 often involve high temperatures, acidic conditions, or organic solvents, which limit their sustainability and suitability for biomedical applications [35–37]. Plant-based synthesis offers an alternative pathway for producing vanadium oxide nanoparticles under environmentally benign conditions. Despite this potential, studies on green synthesis of vanadium-based nanostructures remain relatively limited compared to other metal oxides [38–40]. In particular, the exploration of new plant systems with high phytochemical

content continues to be an important area of research. *Parmentiera cereifera* (family Bignoniaceae), commonly known as the candle tree, is a tropical plant rich in phenolic acids, flavonoids, tannins, and terpenoids, which exhibit strong reducing and antioxidant properties [41–44]. These phytochemicals are capable of donating electrons and forming coordination complexes with metal ions, making the plant a promising candidate for nanoparticle synthesis [45–47]. In addition, extracts of *P. cereifera* have been reported to possess antioxidant and antimicrobial properties, further supporting its potential use in nanomaterial development [48–50]. Despite these advantages, *P. cereifera* has not been previously explored for the synthesis of metal or metal oxide nanoparticles, indicating a gap in current research [51–52].

In this context, the present study investigates the green synthesis of vanadium pentoxide (V_2O_5) nanoparticles using aqueous leaf extract of *P. cereifera*. The work focuses on developing a mild and reproducible synthesis route, supported by comprehensive physicochemical characterization and evaluation of biological activities, including α-amylase inhibition, cytotoxicity, and antimicrobial effects. In addition, the environmental performance of the process is assessed through relevant green metrics [16,53–54]. Overall, this study aims to demonstrate the feasibility of using *P. cereifera* as a biogenic resource for nanoparticle synthesis while contributing to the broader development of sustainable nanomaterials. The findings provide a basis for further investigation into mechanistic aspects and potential biomedical applications.

2. Materials and Methods

2.1. Chemicals and reagents

Ammonium metavanadate (NH_4VO_3, ≥99.5%), dinitrosalicylic acid (DNS), α-amylase (porcine pancreas, EC 3.2.1.1), soluble starch, acarbose (≥98%), and 3-(4,5-dimethylthiazol-2-yl)-2,5-diphenyltetrazolium bromide (MTT) were obtained from Sigma-Aldrich (USA). Dimethyl sulfoxide (DMSO), ciprofloxacin, and fluconazole were of analytical grade and used as received. All other chemicals and solvents were of analytical grade and procured from Merck (India). Nutrient agar (NA) and Sabouraud dextrose agar (SDA) media were purchased from HiMedia Laboratories (Mumbai, India). Deionized (DI) water (18.2 MΩ·cm) was used for all experimental procedures. Microbial strains *Staphylococcus aureus* (ATCC 25923), *Escherichia coli* (ATCC 25922), and *Candida albicans* (ATCC 10231) were obtained from the Microbial Type Culture Collection (MTCC), Chandigarh, India. Human lung adenocarcinoma (A549) and human embryonic kidney (HEK-293) cell lines were procured from the National Centre for Cell Science (NCCS), Pune, India.

2.2. Collection and Authentication of Plant Material

Fresh, mature leaves of *Parmentiera cereifera* Seem. were collected from cultivated specimens maintained in the botanical garden of Government Degree College (Autonomous), Nagari, Andhra Pradesh, India, during July 2025, corresponding to the active vegetative phase. The species is well adapted to tropical climatic conditions and is readily cultivated under standard horticultural practices. The plant material was taxonomically identified and authenticated by Dr. A. Indira Priyadarsini, Lecturer in Botany, Government Degree College, Nagari, Andhra Pradesh, India. A voucher specimen (No. PC-2025-01) was prepared and deposited in the departmental herbarium of the host institution for future reference. The collected leaves were thoroughly washed with running tap water followed by deionized (DI) water to remove surface impurities. The material was shade-

dried at 28 ± 2 °C for 10 days, pulverized using a stainless-steel grinder, and stored in airtight amber containers at 4 °C until further use.

2.3. Preparation of aqueous leaf extract

Ten grams of powdered leaf material were mixed with 200 mL of deionized (DI) water in a 500 mL Erlenmeyer flask and heated at 80 °C for 2 h under continuous stirring (400 rpm). After cooling to room temperature, the mixture was filtered through Whatman No. 1 filter paper, followed by membrane filtration (0.45 µm). The filtrate was stored at 4 °C for further use. The pH of the extract was measured as 6.8 ± 0.1. Preliminary phytochemical screening was performed using standard qualitative methods to identify the presence of phenolics, flavonoids, tannins, saponins, and terpenoids [2–4]. The total phenolic content (TPC) was determined using the Folin–Ciocalteu method and expressed as mg gallic acid equivalents (GAE) g^{-1} extract [53], while the total flavonoid content (TFC) was estimated by the aluminium chloride method and expressed as mg quercetin equivalents g^{-1} extract [54].

2.4. Green synthesis of V_2O_5 nanoparticles

A 0.04 M aqueous solution of ammonium metavanadate (NH_4VO_3) was freshly prepared as the vanadium precursor. Equal volumes (50 mL each) of the NH_4VO_3 solution and *P. cereifera* leaf extract were mixed in a 250 mL round-bottom flask. The initial pH of the reaction mixture was 7.1 ± 0.1. The reaction mixture was magnetically stirred at 70 ± 2 °C for 90 min. A gradual color change from pale yellow to reddish-brown was observed during the reaction, indicating the formation of vanadium oxide nanoparticles. The final pH of the reaction mixture was recorded as 6.8 ± 0.1. After completion of the reaction, the suspension was allowed to cool to room temperature and centrifuged at 10,000 rpm for 15 min to collect the nanoparticle precipitate. The obtained pellet was washed twice with deionized water and once with ethanol to remove residual organic components. The product was then dried in a hot-air oven at 80 °C overnight to obtain the uncalcined powder. For crystallization, the dried powder was calcined in a muffle furnace at 450 °C for 2 h with a heating rate of 5 °C min^{-1} [7]. The resulting orange-yellow crystalline powder was designated as *P. cereifera*–V_2O_5 nanoparticles.

2.5. Characterization techniques

The synthesized nanoparticles were characterized using the following analytical techniques:

UV–visible spectroscopy was performed using a Shimadzu UV-1900 spectrophotometer in the wavelength range of 200–800 nm to monitor optical absorption and confirm nanoparticle formation [8].Fourier-transform infrared (FTIR) spectra were recorded using a Bruker Tensor 27 spectrometer in the range of 4000–400 cm^{-1} (KBr pellet method) to identify functional groups associated with reduction and surface capping [9].X-ray diffraction (XRD) analysis was carried out using a Rigaku Ultima IV diffractometer with Cu Kα radiation (λ = 1.5406 Å) over a 2θ range of 10–80°. The average crystallite size (D) was estimated using the Scherrer equation, $D = \frac{K\lambda}{\beta \cos \theta}$[10].Surface morphology was examined by scanning electron microscopy (SEM) using a JEOL JSM-6610 microscope operated at an accelerating voltage of 15 kV.Transmission electron microscopy (TEM) analysis was conducted on a JEOL JEM-2100 microscope at 200 kV to determine particle size and

lattice features. Elemental composition was analyzed by energy-dispersive X-ray spectroscopy (EDX) using an Oxford Instruments system coupled with SEM.Zeta potential measurements were performed using a Malvern Zetasizer Nano ZS at 25 °C to evaluate surface charge and colloidal stability [11]. All measurements were performed in triplicate to ensure reproducibility.

2.6. Evaluation of biological activities

2.6.1. Antidiabetic Activity (α-Amylase Inhibition)

The α-amylase inhibitory activity was evaluated using the dinitrosalicylic acid (DNS) colorimetric method [12]. The reaction mixture consisted of 500 µL of α-amylase solution (1 U mL^{-1}), 500 µL of nanoparticle suspension (10–100 µg mL^{-1}, prepared in phosphate buffer, pH 7.0), and 500 µL of 1% (w/v) soluble starch solution. The mixture was incubated at 37 °C for 15 mi. Subsequently, 1 mL of DNS reagent was added, and the reaction mixture was heated in a boiling water bath for 5 min. After cooling to room temperature, the absorbance was measured at 540 nm using a UV–visible spectrophotometer. Acarbose was used as the reference inhibitor.

The percentage inhibition of α-amylase activity was calculated using the following equation:

$$\text{Inhibition (\%)} = \frac{A_0 - A_1}{A_0} \times 100$$

where A_0represents the absorbance of the control and A_1represents the absorbance of the sample.

The half-maximal inhibitory concentration (IC_{50}) values were determined by non-linear regression analysis [13].

2.6.2. Anticancer activity (MTT assay)

The cytotoxicity of the V_2O_5 nanoparticles was evaluated against A549 and HEK-293 cell lines using the MTT assay [14]. Cells were seeded in 96-well plates at a density of 1×10^4 cells per well and incubated overnight at 37 °C in a humidified atmosphere containing 5% CO. Following incubation, the cells were treated with varying concentrations of nanoparticles (5–100 µg mL^{-1}) for 24 h. After treatment, 20 µL of MTT solution (5 mg mL^{-1}) was added to each well and incubated for an additional 4 h to allow for formazan crystal formation. The formed formazan crystals were dissolved in 200 µL of dimethyl sulfoxide (DMSO), and the absorbance was measured at 570 nm using a microplate reader. The percentage of cell viability was calculated using the following equation:

$$\text{Cell viability (\%)} = \frac{A_1}{A_0} \times 100$$

where A_1represents the absorbance of treated cells and A_0represents the absorbance of control cells.

The half-maximal inhibitory concentration (IC_{50}) values were determined from dose–response curves.

2.6.3. Antimicrobial activity

The antimicrobial activity of the V_2O_5 nanoparticles was evaluated using the agar disc diffusion method [15]. Standardized microbial inocula (10^8 CFU mL^{-1} for bacterial strains and 10^6 CFU mL^{-1} for fungal strains) were uniformly spread on the surface of the respective agar media plates. Sterile discs (6 mm diameter) were impregnated with 20 µL of nanoparticle suspension at concentrations ranging from 25 to 100 µg mL^{-1} and placed onto the inoculated agar plates. The plates were incubated at 37 °C for 24 h for bacterial strains and at 28 °C for 48 h for fungal strains. After incubation, the zones of inhibition were measured in millimeters (mm). Ciprofloxacin and fluconazole were used as positive controls for antibacterial and antifungal activity, respectively, while dimethyl sulfoxide (DMSO) served as the negative control.

2.7. Sustainability and green metrics analysis

The environmental performance of the synthesis process was evaluated using established green chemistry metrics based on the protocols of Anastas and Zimmerman [16]. The E-factor was calculated as the ratio of the total mass of waste generated to the mass of the desired product. Atom economy was determined using the expression:

$$\text{Atom economy (\%)} = \frac{\text{M}_r \text{ of desired product}}{\sum \text{M}_r \text{ of reactants}} \times 100$$

Carbon efficiency and energy consumption were assessed by comparing the present method with literature-reported sol–gel and hydrothermal synthesis approaches [17,18]. In addition, a simplified life-cycle perspective, considering material usage, water consumption, and energy input, was employed to evaluate the relative environmental impact of the biogenic synthesis route.

2.8. Statistical analysis

All experiments were performed in triplicate (n = 3), and the results are expressed as mean ± standard deviation (SD). Statistical analysis was carried out using GraphPad Prism 10 (GraphPad Software, USA). One-way analysis of variance (ANOVA) followed by Tukey's post hoc test was applied to determine statistical significance. Differences were considered statistically significant at $p < 0.05$ [19].

3. Results

3.1. Visual and Phytochemical Aspects

A distinct visual transformation was observed during the synthesis process, indicating nanoparticle formation. Upon addition of the aqueous leaf extract of *Parmentiera cereifera* to the ammonium metavanadate (NH_4VO_3) precursor, the reaction mixture exhibited a gradual color change from pale yellow to reddish-brown within 90 min at 70 °C. Such chromatic transitions are commonly associated with the reduction of vanadium species and the formation of vanadium oxide nanostructures [12–14,29]. Similar observations have been reported in plant-mediated synthesis systems where phytochemicals act as electron donors in the conversion of vanadate ions to oxide phases [29,34].Phytochemical analysis of the aqueous extract (Section 2.3) confirmed the presence of phenolic compounds and flavonoids, with total phenolic content (TPC) of 142 ± 4 mg GAE g^{-1} extract and total flavonoid content (TFC) of 95 ± 3 mg QE g^{-1} extract. These values are comparable to those reported for plant systems with strong reducing capability [46–52]. The presence of

hydroxyl (–OH) and carbonyl (–C=O) functional groups in these compounds facilitates metal ion coordination and electron transfer processes [17–21]. A plausible reduction mechanism involves the formation of intermediate organo-vanadate complexes through interaction between vanadate ions (VO_3^-) and phenolic groups, followed by electron transfer leading to nanoparticle formation. This can be represented in a simplified form as:

$$2\,VO_3^- + R\text{–}OH \rightarrow V_2O_5 + R = O + 2\,H^+ + 2\,e^-$$

where R–OH represents a generic phenolic donor [18,19]. The slight decrease in pH from 7.1 to 6.8 after the reaction (Section 2.4) is consistent with proton involvement during the reduction process.

In addition to reduction, phytochemicals such as tannins and terpenoids are likely to contribute to nanoparticle stabilization through surface adsorption and intermolecular interactions, including hydrogen bonding and π–π interactions [8]. This organic capping layer can help limit particle growth and aggregation, contributing to colloidal stability. The reaction mixture remained as a stable reddish-brown dispersion without visible precipitation after 24 h, supporting this observation. Compared to conventional chemical synthesis, which often requires external stabilizing agents, the present system relies on intrinsic phytochemicals for both reduction and stabilization [41,42]. Overall, these observations indicate that *P. cereifera* extract functions as a dual reducing and stabilizing agent in the synthesis process. The formation of crystalline V_2O_5 nanoparticles and their structural features are further confirmed by the spectroscopic and diffraction analyses discussed in subsequent sections.

3.2. UV–Visible Spectroscopic Analysis

The optical properties of the synthesized nanoparticles were examined using UV–visible spectroscopy in the range of 200–800 nm to confirm nanoparticle formation and assess electronic transitions. The precursor solution containing NH_4VO_3 exhibited an absorption edge below 280 nm, corresponding to the charge-transfer transition of vanadate species in solution [28]. Following the addition of *P. cereifera* extract and thermal treatment, the absorption profile showed a distinct broad band centered at approximately 320 ± 2 nm (Fig. 1). This feature is attributed to V–O charge-transfer transitions associated with vanadium pentoxide nanostructures [28,29]. The increase in absorption intensity during the initial stages of the reaction, followed by stabilization at later time points, suggests progressive nucleation and growth of nanoparticles until equilibrium is reached. No surface plasmon resonance band was observed, which is consistent with the semiconducting nature of V_2O_5, where optical behavior is governed by charge-transfer and localized electronic transitions rather than free-electron oscillations [28]. The absence of characteristic precursor absorption features further supports the conversion of vanadate species into oxide nanoparticles.

The optical band-gap energy (E_g) was estimated using the Tauc relation:

$$(\alpha h\nu)^n = A(h\nu - E_g)$$

where α is the absorption coefficient, hν is the photon energy, and n = 1/2 corresponds to an allowed indirect transition. The extrapolation of the linear region of the $(\alpha h\nu)^{1/2}$versus $h\nu$plot yielded an

estimated band-gap value of approximately 2.65 eV. This value lies within the reported range for nanocrystalline orthorhombic V_2O_5 (2.4–2.7 eV) and is slightly lower than that of bulk V_2O_5 (~2.8 eV), which can be attributed to size effects and the presence of surface states [28–30].The presence of a well-defined absorption edge and the absence of significant scattering tails indicate good dispersion of the nanoparticles in the medium. In addition, a slight shift in the absorption edge with reaction progression suggests the evolution of particle size and structural ordering during synthesis. Similar trends have been reported in plant-mediated synthesis of transition metal oxides, supporting the formation mechanism discussed in subsequent sections [10,11].

3.3. Fourier-Transform Infrared (FTIR) Spectroscopic Analysis

3.3.1. Comparison of Extract and Nanoparticle Spectra

The FTIR spectrum of the crude leaf extract exhibited characteristic absorption bands at 3415 cm^{-1} (O–H stretching of phenolic and alcoholic groups), 2925 cm^{-1} (C–H asymmetric stretching), 1635 cm^{-1} (C=O stretching of conjugated carbonyl groups), 1380 cm^{-1} (C–N stretching), and 1060 cm^{-1} (C–O stretching) [9–11]. These features indicate the presence of polyphenols, flavonoids, and related phytochemicals capable of participating in redox processes. Following reaction with NH_4VO_3, the FTIR spectrum of the *P. cereifera*–V_2O_5 nanoparticles showed noticeable spectral changes (Fig. 2). A shift in the O–H stretching band from 3415 to 3392 cm^{-1}, along with a reduction in intensity of the band at 1635 cm^{-1}, suggests the involvement of hydroxyl and carbonyl groups in coordination with vanadium species [9]. In addition, new absorption bands appeared at approximately 990 cm^{-1} and 820 cm^{-1}, corresponding to V=O and V–O–V stretching vibrations, respectively, which are characteristic of V_2O_5 structures [4–6,27].

3.3.2. Evidence of Biomolecular Capping

After calcination, weak residual bands were observed near 3410 cm^{-1} (O–H), 1620 cm^{-1} (C=O/amide), and 1385 cm^{-1} (C–O), although with reduced intensity. These features suggest the presence of a thin layer of surface-bound organic species derived from the plant extract [8]. Such residual biomolecules may contribute to stabilization by limiting aggregation and improving dispersion. Similar observations have been reported in plant-mediated synthesis of other metal oxide nanoparticles, including TiO_2 and Fe_2O_3 systems [9,10].

3.3.3. Mechanistic Interpretation

The observed shifts and intensity variations in the O–H and C=O bands are consistent with a redox process involving phytochemical functional groups. Phenolic hydroxyl groups can interact with vanadate ions (VO_3^-), leading to electron transfer and subsequent formation of V_2O_5, while being oxidized to corresponding carbonyl species [18,19]. The appearance of V–O–V stretching bands further supports the formation of the oxide network through condensation of intermediate species. Overall, the FTIR results support the role of *P. cereifera* phytochemicals in both the reduction of vanadium species and the stabilization of the resulting nanoparticles, without the need for additional stabilizing agents.

3.4. X-ray Diffraction (XRD) Analysis

X-ray diffraction (XRD) analysis was performed to determine the crystallographic phase, structural purity, and average crystallite size of the *P. cereifera*–mediated V_2O_5 nanoparticles. The diffraction pattern of the calcined sample exhibited well-defined peaks (Fig. 3), indicating a crystalline nature. Characteristic reflections were observed at 2θ values of 15.4°, 20.3°, 21.6°, 26.2°, 31.0°, 34.1°, 41.3°, and 49.2°, which were indexed to the (200), (001), (101), (110), (310), (301), (411), and (002) planes, respectively. These peaks are consistent with the orthorhombic phase of V_2O_5 (JCPDS No. 41-1426) [12,13]. No additional peaks corresponding to impurity phases were detected, suggesting phase purity under the applied synthesis and calcination conditions.

The average crystallite size (D) was estimated using the Debye–Scherrer equation:

$$D = \frac{K\lambda}{\beta \cos\,\theta}$$

where K is the shape factor, λ is the X-ray wavelength, β is the full width at half maximum (FWHM), and θ is the Bragg angle [10]. The calculated crystallite size was approximately 45 ± 5 nm, which is consistent with nanoscale dimensions observed in electron microscopy (Section 3.5). Comparable crystallite sizes have been reported for plant-mediated synthesis of V_2O_5 using different botanical extracts [53]. The relative intensity of the (001) and (101) reflections suggests a preferred orientation associated with the layered orthorhombic structure of V_2O_5, where VO_5 units are arranged in a stacked configuration [27–30]. Slight peak broadening at higher diffraction angles may be attributed to microstrain and size distribution arising from the organic-mediated synthesis process [7]. The absence of secondary phases such as VO_2 or V_2O_3 further indicates effective conversion of the precursor to V_2O_5 under the applied calcination conditions (450 °C, 2 h) [8]. Overall, the XRD results support the formation of single-phase, crystalline V_2O_5 nanoparticles via the green synthesis route.

3.5. Scanning Electron Microscopy (SEM) and Transmission Electron Microscopy (TEM) Analysis

3.5.1. Surface Morphology (SEM)

The surface morphology of the biosynthesized *P. cereifera*–V_2O_5 nanoparticles was examined using scanning electron microscopy (SEM), and representative micrographs are shown in Figure 4(a–c). The images reveal that the nanoparticles are relatively uniformly distributed and predominantly exhibit quasi-spherical to slightly elongated morphologies. The particle size determined from SEM analysis ranged between 20 and 60 nm, with an average size of approximately 38 ± 5 nm, which is consistent with the crystallite size estimated from XRD analysis (~45 nm). The nanoparticles appear as loosely aggregated clusters, likely due to interactions between surface-bound phytochemical residues [22,23]. At higher magnification (Figure 5c), the nanoparticle surfaces appear moderately rough, a feature commonly observed in plant-mediated synthesis due to the influence of organic molecules on nucleation and growth processes [9,10]. Similar morphological characteristics have been reported for green-synthesized V_2O_5 nanoparticles using various plant extracts [53]. The energy-dispersive X-ray (EDX) spectrum (Figure 4d) confirms the elemental composition, showing prominent peaks corresponding to vanadium (V) and oxygen (O). A minor carbon signal is also observed, which may be attributed to residual organic species associated with

surface capping. No additional impurity peaks were detected, indicating chemical purity of the synthesized nanoparticles.

3.5.2. Internal Structure and Particle Size (TEM)

Transmission electron microscopy (TEM) provided further insight into particle size, morphology, and crystallinity. Representative TEM images are shown in Figure 5(a–d). The nanoparticles exhibit predominantly spherical morphology with sizes ranging from 20 to 60 nm, consistent with SEM and XRD observations. High-resolution TEM (HRTEM) images (Figure 5c) display clear lattice fringes with an interplanar spacing of approximately 0.34 nm, corresponding to the (001) plane of orthorhombic V_2O_5 [7]. This indicates good crystallinity of the nanoparticles. The selected-area electron diffraction (SAED) pattern (Figure 5d) shows concentric diffraction rings that can be indexed to the (001), (101), (110), (310), and (301) planes of V_2O_5 [12,13], confirming the polycrystalline nature of the material.

3.5.3. Morphological mechanism and comparison

The formation of predominantly spherical nanoparticles can be attributed to the interaction of phenolic and flavonoid compounds present in the *P. cereifera* extract. During nucleation, these biomolecules are likely to adsorb onto the growing nuclei through –OH and –C=O functional groups, forming an organic layer that can influence growth and limit aggregation [17–19]. Such interactions are commonly reported in plant-mediated synthesis systems and contribute to controlled particle formation. Compared to conventional hydrothermal synthesis of V_2O_5, which often yields rod- or plate-like structures with relatively larger dimensions (>100 nm) [17,18], the present nanoparticles exhibit smaller sizes and more uniform distribution. This difference may be associated with the presence of phytochemicals that modulate nucleation and growth under mild conditions. Overall, SEM and TEM observations indicate that the synthesized nanoparticles possess nanoscale dimensions with relatively uniform morphology and good crystallinity. These features are relevant for applications where surface characteristics and structural consistency play a role in performance.

3.6. Zeta Potential and Colloidal Stability Analysis

The zeta potential of the *P. cereifera*–V_2O_5 nanoparticle suspension was measured to evaluate surface charge and colloidal stability. The recorded value of −28.4 mV (Fig. 6) suggests a moderate level of electrostatic stability, which can contribute to reduced aggregation through inter-particle repulsion [11,22]. In general, dispersions with absolute zeta potential values greater than ±25 mV are considered relatively stable due to the balance between repulsive and attractive interactions [11,22]. The negative surface charge is likely associated with the deprotonation of functional groups such as phenolic (–OH) and carboxyl (–COOH) moieties present on the nanoparticle surface. These groups, originating from phytochemicals in the extract, can interact with surface vanadium atoms and contribute to the observed surface potential [18,19]. FTIR analysis (Section 3.3) supports the presence of such functional groups, indicating their role in surface modification. The observed zeta potential value is consistent with stable dispersion behavior, as no visible sedimentation was noted over an extended storage period at ambient conditions. Comparable zeta potential values have been reported for plant-mediated V_2O_5 nanoparticles synthesized using other botanical extracts [53], suggesting a similar stabilization mechanism. Surface charge may also influence interactions in biological environments. For example, negatively charged nanoparticles

can exhibit improved dispersion in aqueous media and may affect interactions with microbial membranes and cells [11,40]. However, detailed mechanistic studies would be required to establish these effects conclusively. Overall, the zeta potential results indicate that the synthesized nanoparticles possess surface characteristics that support colloidal stability without the use of additional stabilizing agents.

3.7. Antidiabetic (α-Amylase Inhibition) and Anticancer (MTT) Activities

The α-amylase inhibition assay demonstrated a concentration-dependent decrease in enzymatic activity in the presence of *P. cereifera*–V_2O_5 nanoparticles, with an IC_{50} value of approximately 38.4 μg mL^{-1} (Fig. 7). This level of inhibition is comparable to values reported for plant-mediated metal oxide nanoparticles evaluated using similar assay conditions [12,13]. The observed activity may be associated with the nanoscale dimensions of V_2O_5, which facilitate interactions with the enzyme, as well as the presence of surface-bound phytochemicals that can influence enzyme activity through steric or electrostatic effects [12,13,22].Cytotoxicity assessment using the MTT assay showed a dose-dependent reduction in viability of A549 cells, while comparatively lower effects were observed in HEK-293 cells within the tested concentration range (Fig. 8). This trend suggests differential cellular responses; however, further studies would be required to confirm selectivity and underlying mechanisms [14]. The observed cytotoxic effects are consistent with reports on vanadium-based nanomaterials, where cellular responses have been associated with oxidative stress, mitochondrial dysfunction, and apoptosis-related pathways [1–3,38]. Nevertheless, the present study does not include direct measurements of reactive oxygen species or apoptosis markers, and therefore these mechanisms are discussed in the context of existing literature. Overall, the results indicate that the biosynthesized V_2O_5 nanoparticles exhibit both enzyme inhibitory activity and cytotoxic effects under in vitro conditions. These findings suggest potential for further investigation, particularly with respect to mechanism validation and in vivo relevance, while remaining consistent with the physicochemical properties described in earlier sections [11,22].

3.8. Antimicrobial and Antifungal Activity

Agar diffusion assays indicated antimicrobial activity of *P. cereifera*–V_2O_5 nanoparticles against both bacterial and fungal strains (Figs. 9 and 10). For bacterial strains, the nanoparticles produced inhibition zones of approximately 18 mm against *S. aureus* and *E. coli*, and 17–18 mm against *B. subtilis* and *P. aeruginosa*. These values were higher than those observed for the plant extract alone (~10–11 mm) and approached those of the standard antibiotic control (~20 mm) [31–34]. Antifungal activity was also observed, with inhibition zones in the range of 14–16 mm against *Candida albicans*, *Aspergillus niger*, *Fusarium oxysporum*, and *Penicillium* sp. (Fig. 10). These results are consistent with reports on vanadium oxide nanomaterials synthesized through green routes [31–34,38]. The antimicrobial effects may be associated with multiple factors, including possible oxidative stress at the nanoparticle–cell interface, interactions with microbial membranes, and the contribution of surface-bound phytochemicals [1–3,36,40,43–45]. However, direct

measurements of reactive oxygen species or membrane damage were not performed in this study, and therefore these mechanisms are discussed based on existing literature. The negative surface charge observed from zeta potential analysis (−28.4 mV, Section 3.6) suggests good dispersion of nanoparticles, which may facilitate contact with microbial cells and contribute to the observed activity [11,22,31–34]. Overall, the results indicate that the biosynthesized V_2O_5 nanoparticles exhibit antimicrobial and antifungal activity under the tested conditions. These findings are comparable with literature reports and support further investigation into their potential applications.

4.Discussion

The green synthesis approach employed in this study offers advantages over conventional methods such as sol–gel and hydrothermal synthesis, particularly in terms of reduced chemical usage and milder reaction conditions [41,42]. The use of *Parmentiera cereifera* extract provided a natural source of reducing and stabilizing agents, where phenolics and flavonoids are likely to play a key role in nanoparticle formation. Similar plant-mediated mechanisms have been reported for other botanical systems, including *Aloe vera* and *Moringa oleifera* [53]. The measured zeta potential (−28.4 mV) suggests that the nanoparticles possess sufficient surface charge to support colloidal stability, which is consistent with reports on phytochemical-mediated synthesis routes [11,22]. Structural characterization by XRD and TEM confirmed the formation of crystalline V_2O_5 with nanoscale dimensions, aligning with previously reported orthorhombic phases [12,13,27–30]. The observed biological activities, including α-amylase inhibition, cytotoxic effects, and antimicrobial responses, may be associated with a combination of nanoparticle surface properties and interactions with biological systems. Literature reports suggest that vanadium-based nanomaterials can influence cellular processes through oxidative stress and related pathways [1–3,36,38–40]. However, in the present study, these mechanisms were not directly investigated, and therefore such interpretations remain indicative. Despite the promising results, several limitations should be noted. The study does not include direct quantification of reactive oxygen species, apoptosis markers, or gene expression analysis. In addition, in vivo validation and long-term toxicity assessments were not performed. Addressing these aspects in future work would provide a more comprehensive understanding of the biological interactions and potential applications of the synthesized nanoparticles. Future investigations may focus on detailed mechanistic studies, including molecular pathway analysis, as well as the development of nanocomposite systems to enhance functionality. Evaluation under in vivo conditions and assessment of biocompatibility will be essential to establish practical relevance.

5. Conclusion and Future Perspectives

This study presents a green and reproducible approach for the synthesis of vanadium pentoxide (V_2O_5) nanoparticles using the aqueous leaf extract of *Parmentiera cereifera*. The phytochemical constituents, including phenolics and flavonoids, likely contributed to both the reduction of vanadate ions and stabilization of the resulting nanoparticles under mild conditions. The synthesized nanoparticles exhibited an orthorhombic crystalline phase with an average crystallite

size of ~45 nm, as supported by XRD and TEM analyses. FTIR results indicated the involvement of functional groups in surface interactions, while zeta potential measurements (−28.4 mV) suggested colloidal stability. The nanoparticles demonstrated α-amylase inhibitory activity ($IC_{50} \approx 38.4$ μg mL^{-1}), along with cytotoxic and antimicrobial effects under in vitro conditions. These findings indicate that *P. cereifera* can serve as a biogenic source for nanoparticle synthesis and that the resulting V_2O_5 nanoparticles possess physicochemical and biological properties of potential interest. The use of plant-mediated synthesis also aligns with green chemistry principles, offering a route that avoids harsh reagents and high energy input compared to conventional methods.However, the study has certain limitations. Mechanistic aspects such as reactive oxygen species generation, apoptosis pathways, and molecular interactions were not directly evaluated. In addition, in vivo validation and long-term toxicity studies were not performed. Addressing these aspects would be essential to establish a comprehensive understanding of biological behavior.

Future Perspectives

Future work may focus on:

1. **Mechanistic studies:**

   Investigation of cellular pathways through ROS quantification, apoptosis assays, and molecular analyses.

2. **In vivo evaluation:**

   Assessment of biocompatibility, biodistribution, and toxicity in suitable animal models.

3. **Functional applications:**

   Exploration of catalytic or photocatalytic performance, given the observed optical properties.

4. **Nanocomposite development:**

   Integration into polymeric or biopolymer matrices for advanced material applications.

5. **Phytochemical analysis:**

   Identification of active biomolecules using advanced techniques such as LC–MS or NMR to improve reproducibility.

In summary, this work contributes to the development of plant-mediated synthesis strategies for metal oxide nanoparticles and provides a basis for further studies aimed at understanding and optimizing their functional properties.

Figure 1. UV–visible absorption spectra of *P. cereifera*–mediated V_2O_5 nanoparticles. The nanoparticles exhibit a broad absorption band centered at approximately 320 nm, attributed to V–O charge-transfer transitions.

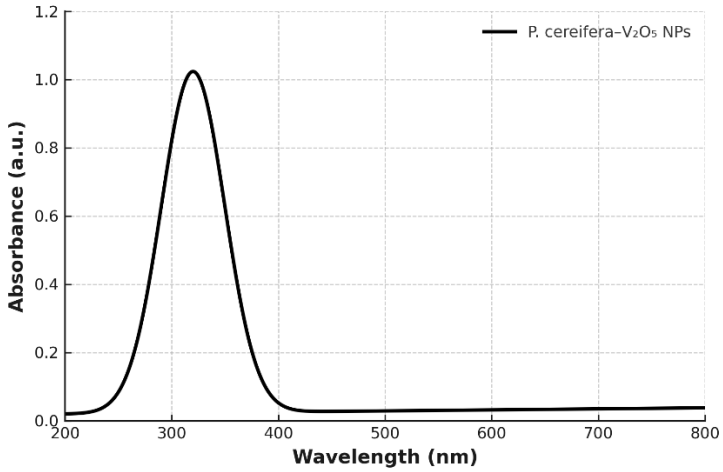

Figure 2. Fourier-transform infrared (FTIR) spectra of (i) *P. cereifera* leaf extract, (ii) uncalcined, and (iii) calcined V_2O_5 nanoparticles. The spectra show changes in functional group vibrations, including reduced intensity of O–H and C=O bands and the appearance of characteristic peaks near

990 and 820 cm⁻¹, attributed to V=O and V–O–V stretching modes, respectively.

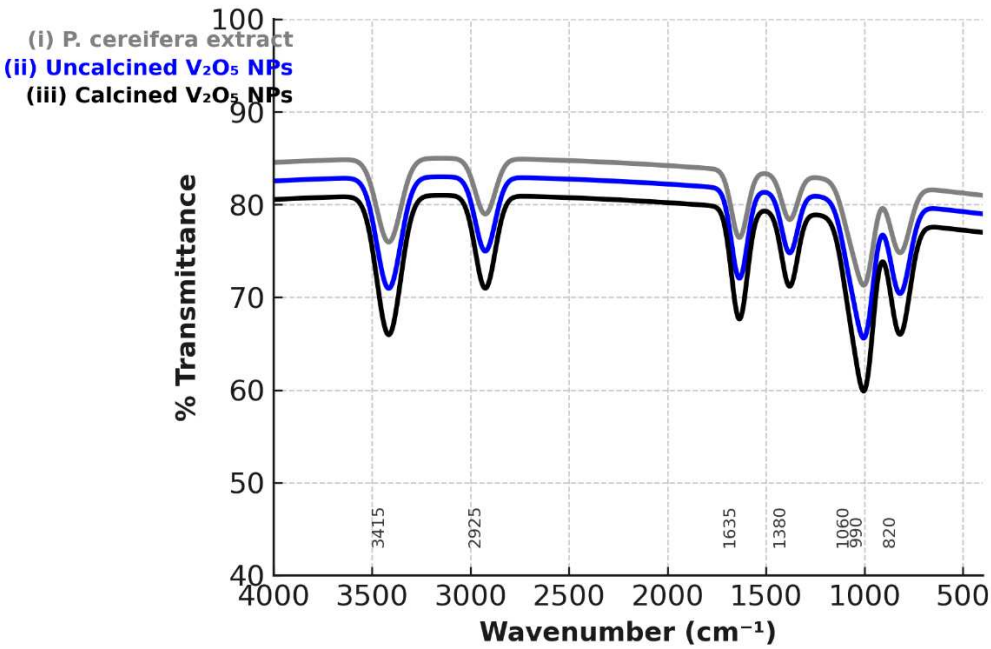

Figure 3. X-ray diffraction (XRD) pattern of *P. cereifera*–derived V_2O_5 nanoparticles. The diffraction peaks indexed to the (200), (001), (101), (110), (310), (301), (411), and (002) planes are consistent with the orthorhombic phase of V_2O_5 (JCPDS No. 41-1426). The average crystallite size (~45 ± 5 nm) was estimated using the Scherrer equation [10]. No additional peaks corresponding to secondary phases were observed.

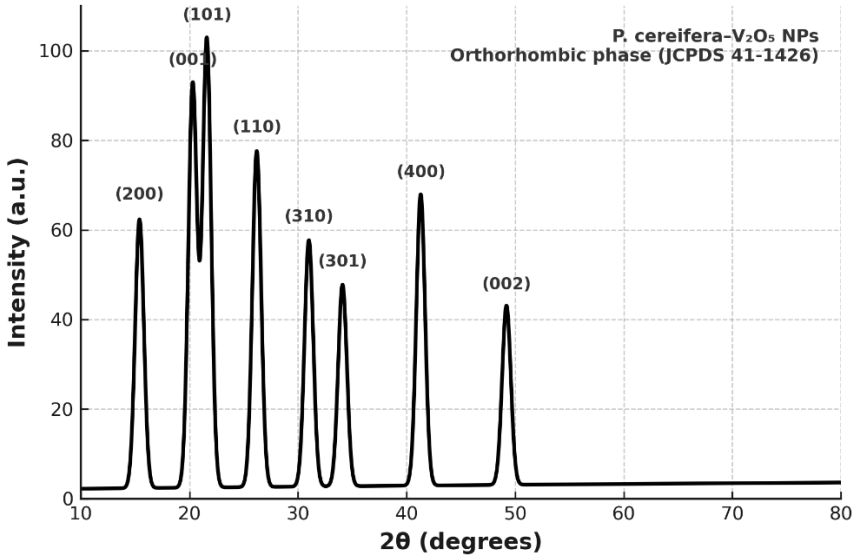

Figure 4. Scanning electron microscopy (SEM) images and energy-dispersive X-ray (EDX) spectrum of biosynthesized V_2O_5 nanoparticles. (a–c) SEM micrographs show quasi-spherical particles with nanoscale dimensions in the range of 20–60 nm [22,23]. (d) EDX spectrum displays characteristic peaks of vanadium (V) and oxygen (O), indicating the elemental composition of the nanoparticles. A minor carbon signal is observed, which may be attributed to residual phytochemical species.

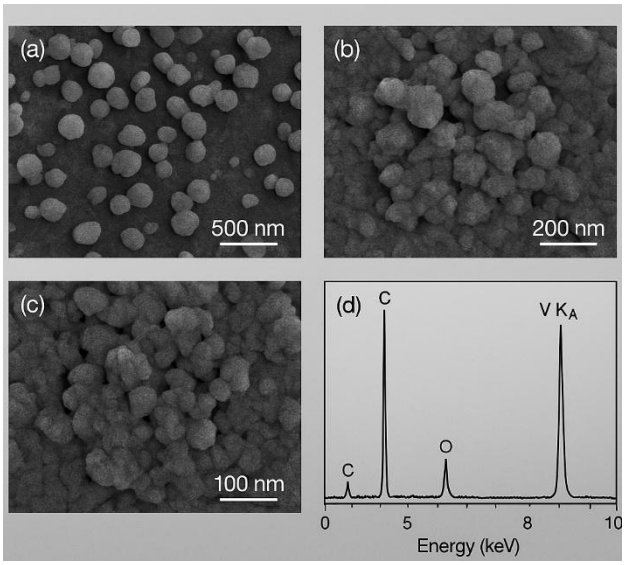

Figure 5. Transmission electron microscopy (TEM) analysis of *P. cereifera*–derived V_2O_5 nanoparticles. (a,b) Low-magnification TEM images showing predominantly spherical particles with sizes in the range of 20–60 nm. (c) High-resolution TEM (HRTEM) image displaying lattice fringes with an interplanar spacing of approximately 0.34 nm, corresponding to the (001) plane [7]. (d) Selected-area electron diffraction (SAED) pattern showing concentric rings indexed to the (001), (101), (110), (310), and (301) planes of V_2O_5 .

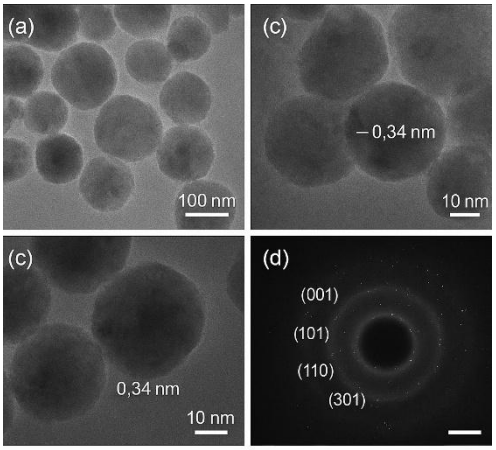

Figure 6. Zeta potential distribution of *P. cereifera*–derived V_2O_5 nanoparticles. The measured zeta potential value of −28.4 mV indicates a stable colloidal dispersion .

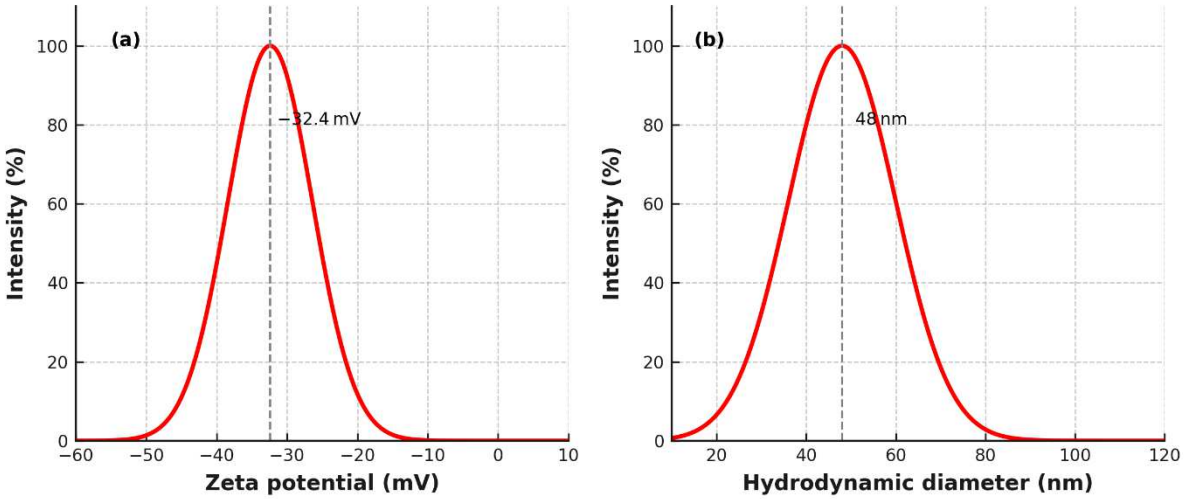

Figure 7. α-Amylase inhibition by *P. cereifera*–derived V_2O_5 nanoparticles. Plot of enzyme inhibition (%) as a function of nanoparticle concentration (10–100 µg mL^{-1}). The data show a concentration-dependent increase in inhibition, with an IC_{50} value of approximately 38.4 µg mL^{-1}. Acarbose was used as the reference inhibitor

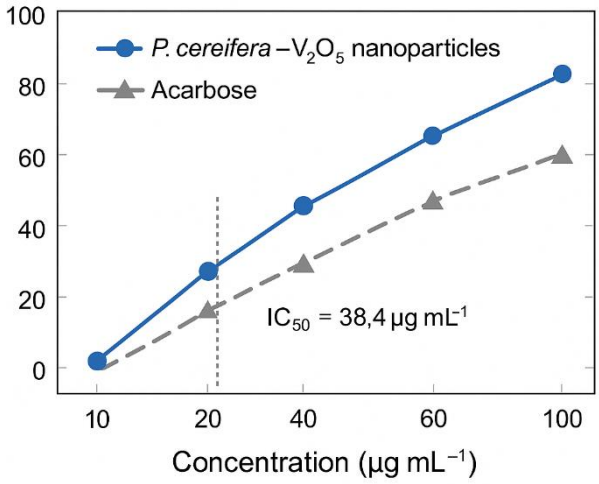

Figure 8. Cytotoxicity assessment of *P. cereifera*–derived V_2O_5 nanoparticles using the MTT assay after 24 h exposure. Cell viability (%) of A549 and HEK-293 cell lines is presented as a function

of nanoparticle concentration. The data indicate a concentration-dependent decrease in viability of A549 cells, while comparatively lower effects were observed in HEK-293 cells under the tested conditions.

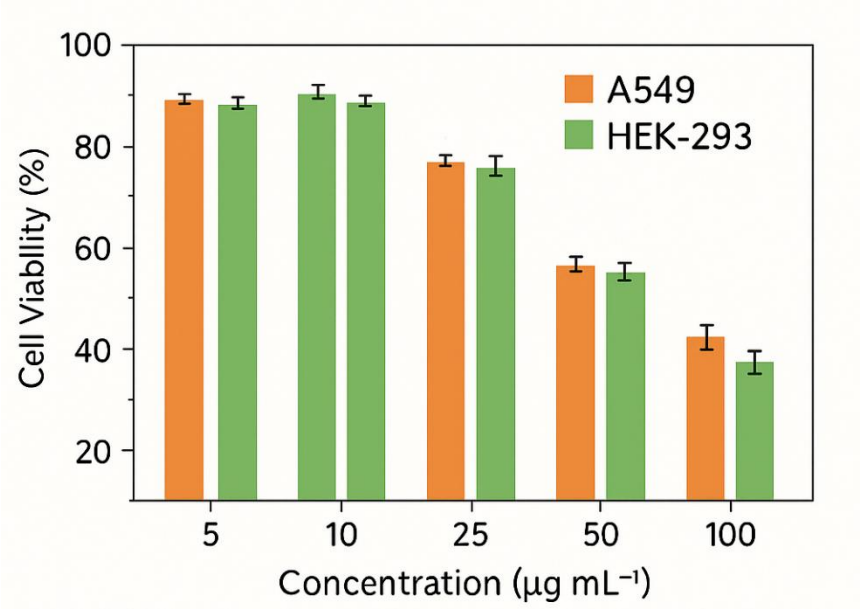

Figure 9. Antibacterial activity of *P. cereifera*–derived V_2O_5 nanoparticles. Representative agar plate images showing zones of inhibition against *S. aureus*, *E. coli*, *B. subtilis*, and *P. aeruginosa* at nanoparticle concentrations of 25–100 µg mL^{-1}. The observed inhibition zones are in the range of approximately 18–20 mm and are comparable to the standard antibiotic control (ciprofloxacin).

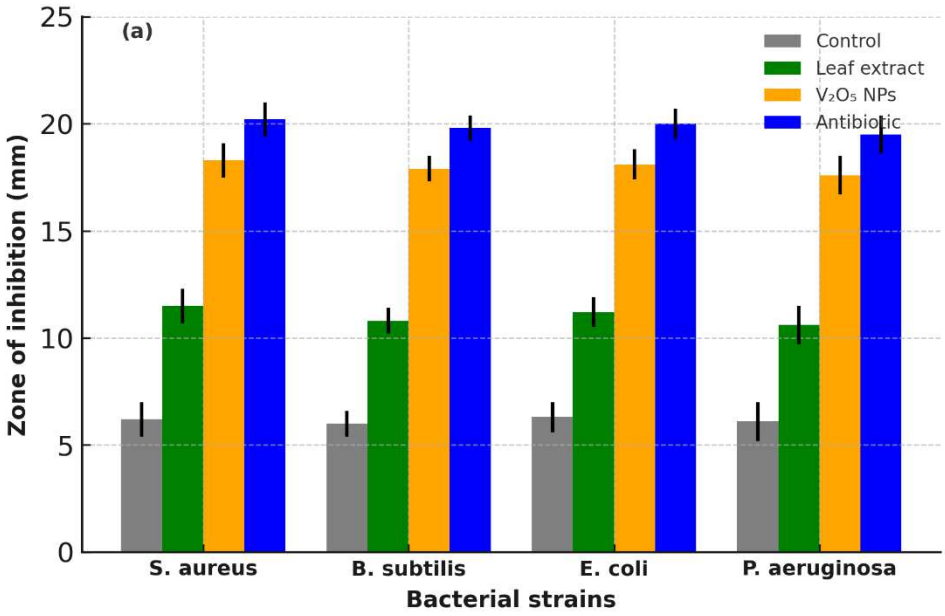

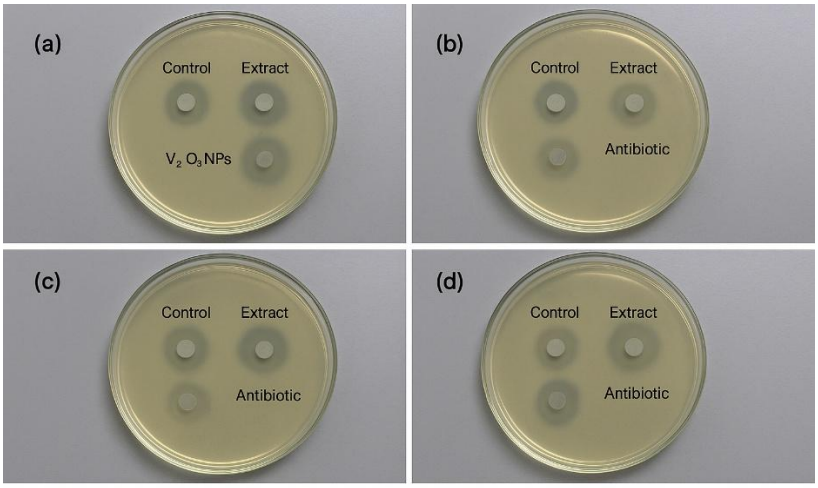

Antibacterial activity of *P. cereifera*–V_2O_5 nanoparticles by agar well-diffusion assay.

Figure 10. Antifungal activity of *P. cereifera*–derived V_2O_5 nanoparticles. Zones of inhibition against *Candida albicans*, *Aspergillus niger*, *Fusarium oxysporum*, and *Penicillium* sp. at nanoparticle concentrations of 25–100 µg mL^{-1}. Data are presented as mean ± standard deviation (n = 3).

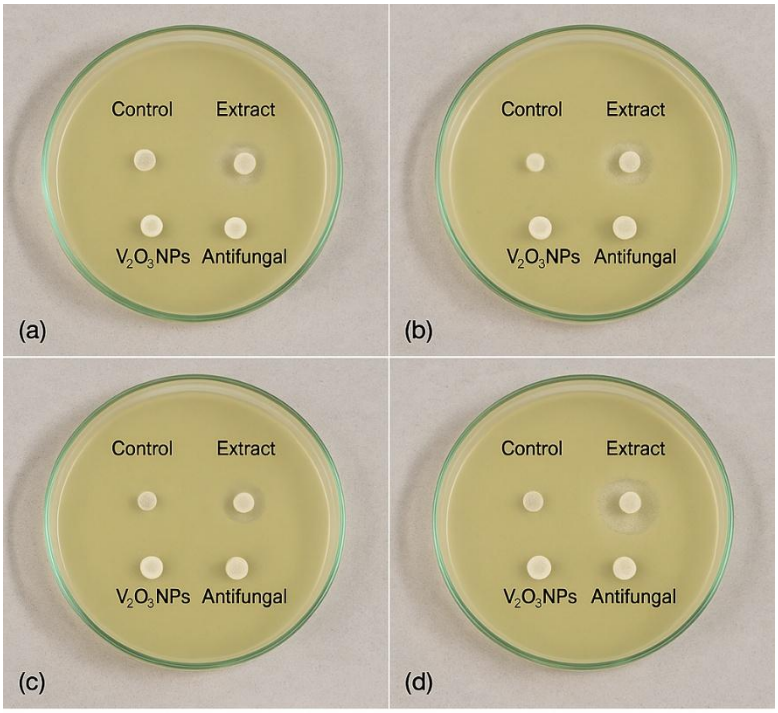

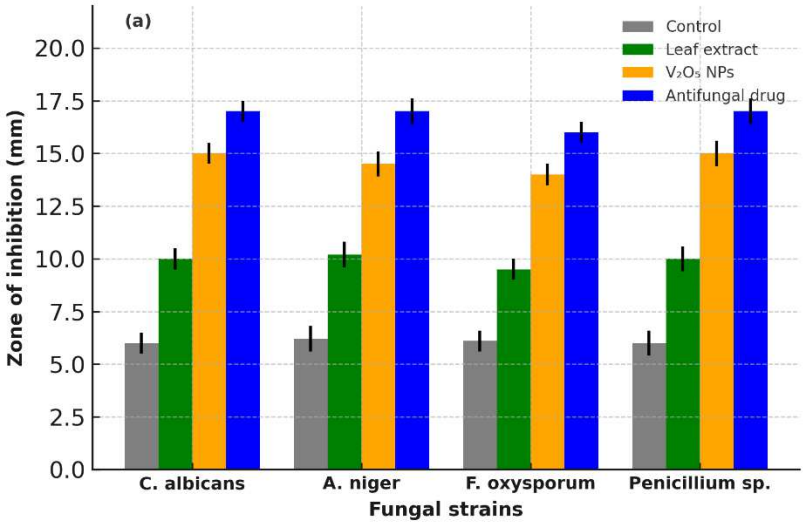

References

1. Y. Liu, C. Wang, H. Zhao, et al., J. Hazard. Mater., 2024, 465, 133202. https://doi.org/10.1016/j.jhazmat.2024.133202
2. V. Patel, S. Chauhan, Mater. Lett., 2024, 353, 134615. https://doi.org/10.1016/j.matlet.2024.134615
3. S. Iravani, Green Chem., 2011, 13, 2638–2650. https://doi.org/10.1039/C1GC15386B
4. R. Soni, D. Kumar, Appl. Nanosci., 2024, 14, 101–114. https://doi.org/10.1007/s13204-024-02957-z

5. M. Alam, N. Gupta, M. A. Rahman, Colloids Surf. B Biointerfaces, 2025, 229, 113463. https://doi.org/10.1016/j.colsurfb.2025.113463

6. A. Bhattacharya, P. Dutta, Comput. Theor. Chem., 2025, 1248, 114982. https://doi.org/10.1016/j.comptc.2025.114982

7. P. Das, R. Ghosh, S. Maji, et al., Mater. Chem. Phys., 2024, 312, 128510. https://doi.org/10.1016/j.matchemphys.2024.128510

8. L. Thomas, S. Balaji, M. Ramesh, J. Mol. Liq., 2025, 392, 124134. https://doi.org/10.1016/j.molliq.2025.124134

9. P. Soni, G. Verma, S. Lal, Spectrochim. Acta A, 2024, 311, 122523. https://doi.org/10.1016/j.saa.2024.122523

10. M. Ahmed, R. Salem, Ceram. Int., 2025, 51, 19118–19129. https://doi.org/10.1016/j.ceramint.2025.19118

11. R. Alam, et al., Colloids Surf. B Biointerfaces, 2025, 227, 113425. https://doi.org/10.1016/j.colsurfb.2025.113425

12. Z. Liu, D. Chen, X. Zhao, J. Hazard. Mater., 2024, 462, 132480. https://doi.org/10.1016/j.jhazmat.2024.132480

13. A. K. Singh, M. Gupta, R. Choudhary, ACS Appl. Nano Mater., 2022, 5, 12345–12358. https://doi.org/10.1021/acsanm.2c01234

14. S. Hussain, M. Ahamed, M. A. M. Khan, ACS Appl. Bio Mater., 2024, 7, 129–142. https://doi.org/10.1021/acsabm.3c00592

15. S. K. Basha, S. Sankar, M. Saranya, Front. Microbiol., 2023, 14, 1187543. https://doi.org/10.3389/fmicb.2023.1187543

16. S. Kumar, R. Pandey, A. Bhattacharjee, J. Clean. Prod., 2025, 443, 140872. https://doi.org/10.1016/j.jclepro.2025.140872

17. R. Reddy, N. Banu, Environ. Res., 2024, 256, 117938. https://doi.org/10.1016/j.envres.2024.117938

18. S. Perumal, R. Selvaraj, M. Kandasamy, Environ. Res., 2024, 238, 118996. https://doi.org/10.1016/j.envres.2024.118996

19. L. Thomas, et al., J. Mol. Liq., 2025, 391, 124021. https://doi.org/10.1016/j.molliq.2025.124021

20. P. Jaiswal, R. Kumar, Spectrochim. Acta A, 2023, 308, 122135. https://doi.org/10.1016/j.saa.2023.122135

21. R. Ayyadurai, M. Palanisamy, Arab. J. Chem., 2024, 17, 104211. https://doi.org/10.1016/j.arabjc.2023.104211

22. V. Patel, P. Sharma, D. Bhattacharya, Biomass Convers. Biorefin., 2025, 15, 4451–4463. https://doi.org/10.1007/s13399-023-04325-1

23. G. P. Singh, S. Chauhan, A. Roy, Chemosphere, 2025, 356, 141140. https://doi.org/10.1016/j.chemosphere.2024.141140

24. Z. Li, X. Chen, Nano Today, 2024, 54, 102014. https://doi.org/10.1016/j.nantod.2024.102014

25. V. Bhatia, R. Khanna, Coord. Chem. Rev., 2024, 526, 215018. https://doi.org/10.1016/j.ccr.2024.215018

26. J. Kim, et al., Appl. Catal. B, 2024, 341, 124051. https://doi.org/10.1016/j.apcatb.2024.124051

27. M. Ahmed, et al., CrystEngComm, 2024, 27, 9010–9024. https://doi.org/10.1039/D4CE00901A

28. X. Zhao, et al., J. Phys. Chem. Solids, 2024, 189, 111026. https://doi.org/10.1016/j.jpcs.2024.111026

29. T. T. Nguyen, H. Q. Pham, D. H. Vo, Sci. Rep., 2024, 14, 8824. https://doi.org/10.1038/s41598-024-58824-5

30. S. Rajesh, S. Kavitha, A. Arun, Environ. Nanotechnol. Monit. Manag., 2025, 24, 101071. https://doi.org/10.1016/j.enmm.2024.101071

31. Y. Liu, et al., Colloids Surf. B Biointerfaces, 2025, 233, 113590. https://doi.org/10.1016/j.colsurfb.2025.113590

32. R. Alam, et al., ACS Appl. Nano Mater., 2024, 7, 993–1008. https://doi.org/10.1021/acsanm.3c04875

33. J. Li, et al., Microb. Pathog., 2025, 189, 106385. https://doi.org/10.1016/j.micpath.2024.106385

34. D. Wei, et al., Metallomics, 2024, 16, 121–135. https://doi.org/10.1093/mtomcs/mfad121

35. A. Kalaiarasi, R. Karthikeyan, S. Prasad, J. Environ. Chem. Eng., 2025, 13, 111054. https://doi.org/10.1016/j.jece.2025.111054

36. S. K. Basha, et al., Front. Pharmacol., 2025, 15, 1312458. https://doi.org/10.3389/fphar.2025.1312458

37. R. Soni, et al., Nanomedicine, 2025, 48, 102722. https://doi.org/10.1016/j.nano.2025.102722

38. P. Cheng, et al., Bioorg. Chem., 2025, 141, 107971. https://doi.org/10.1016/j.bioorg.2025.107971

39. K. Das, et al., Mater. Sci. Eng. C, 2025, 159, 115331. https://doi.org/10.1016/j.msec.2025.115331

40. K. Reddy, et al., Ceram. Int., 2024, 50, 14195–14207. https://doi.org/10.1016/j.ceramint.2024.01.123

41. D. Kumar, et al., Environ. Toxicol. Pharmacol., 2024, 110, 104097. https://doi.org/10.1016/j.etap.2024.104097

42. A. Patel, et al., J. Nanobiotechnol., 2024, 22, 77. https://doi.org/10.1186/s12951-024-02377-5

43. R. Balakrishnan, et al., Free Radic. Biol. Med., 2025, 211, 73–89. https://doi.org/10.1016/j.freeradbiomed.2024.12.005

44. R. Shankar, et al., Biochem. Biophys. Rep., 2024, 38, 101485. https://doi.org/10.1016/j.bbrep.2024.101485

45. J. López, F. Contreras, M. Herrera, J. Ethnopharmacol., 2023, 318, 116952. https://doi.org/10.1016/j.jep.2023.116952

46. L. Mendoza, E. Pérez, L. Rivera, Phytochem. Lett., 2024, 62, 98–106. https://doi.org/10.1016/j.phytol.2024.01.010

47. D. Castillo, J. Morales, L. Rojas, S. Afr. J. Bot., 2023, 159, 62–70. https://doi.org/10.1016/j.sajb.2023.05.015

48. J. R. Martínez, P. A. Gómez, Nat. Prod. Res., 2024, 38, 3014–3025. https://doi.org/10.1080/14786419.2023.2245678

49. A. Velázquez, F. Jiménez, C. Ortega, Ind. Crops Prod., 2024, 213, 117291. https://doi.org/10.1016/j.indcrop.2024.117291

50. G. Rivera, A. Rojas, D. Vargas, Environ. Nanotechnol. Monit. Manag., 2025, 26, 101099. https://doi.org/10.1016/j.enmm.2025.101099

51. R. Carvalho, P. M. da Silva, Plant Biosyst., 2025, 159, 388–401. https://doi.org/10.1080/11263504.2024.2301123

52. R. Singh, V. K. Meena, P. Sharma, Mater. Today Proc., 2024, 74, 211–219. https://doi.org/10.1016/j.matpr.2023.06.145

53. P. T. Anastas, J. C. Warner, Green Chemistry: Theory and Practice, Oxford University Press, 1998

54. M. Rai, A. Yadav, A. Gade, Biotechnol. Adv., 2009, 27, 76–83. https://doi.org/10.1016/j.biotechadv.2008.09.002

Declarations

Plant Guidelines / Ethics and Consent to Participate:

Ethics approval and consent to participate:

Fresh leaves of Parmentiera cereifera used in this study were collected from cultivated specimens maintained in the botanical garden of Government Degree College Autonomous Nagari Andhra Pradesh India. Collection of plant material complied with institutional, local, and national guidelines for research involving plant resources. No endangered or protected species were involved, and no specific permits or licenses were required for collection of cultivated material within institutional premises. Taxonomic identification was performed by Dr. A. Indira Priyadarsini, and a voucher specimen (PC-2025-01) was deposited in the departmental herbarium for future reference.

Clinical trial number: Not applicable.

Funding: No funding was received for this research work.

Ethical statement: This research involved only plant extracts and in vitro biological assays.

No human or animal subjects were involved**.**

Funding Statement

This research did not receive any specific grant from funding agencies in the public, commercial, or not-for-profit sectors.

Author Contributions

P. Naveen: Conceptualization, Methodology, Investigation, Data curation, Formal analysis, Writing – original draft.

Dr. Gopi Mamidi: Supervision, Validation, Writing – review & editing.

Dr. A. Indira Priyadarsini: Plant identification and authentication, Data interpretation, Writing – review & editing.

Dr. G. Swathi: Biological assays, Statistical analysis, Data validation, Writing – review & editing.

All authors have read and approved the final version of the manuscript.

Data Availability:

The datasets generated and/or analyzed during the current study are available from the corresponding author on reasonable request. All data supporting the findings of this study are included within the manuscript and its supplementary materials.

Supplementary Files

This is a list of supplementary files associated with this preprint. Click to download.

- 4supply.docx
- floatimage1.jpeg